Adhesion Maturation of Neutrophils on Nanoscopically Presented Platelet Glycoprotein Ibα

Sebastian Kruss,[†,∥] Luise Erpenbeck,[‡,∥] Katharina Amschler,[‡] Tabea A. Mundinger,[†] Heike Boehm,[†] Hans-Joachim Helms,[§] Tim Friede,[§] Robert K. Andrews,[⊥] Michael P. Schön,[‡,∥,*] and Joachim P. Spatz[†,∥,*]

[†]Department of New Materials and Biosystems, Max Planck Institute for Intelligent Systems, and Institute of Physical Chemistry, Heidelberg University, Heisenbergstraße 3, Stuttgart 70569, Germany, [‡]Department of Dermatology, Venereology and Allergology, University Medical Center Göttingen, 40 Robert-Koch-Straße, Göttingen 37075, Germany, [§]Department of Medical Statistics, University Medical Center Göttingen, 32 Humboldtallee, Göttingen 37073, Germany, and [⊥]Australian Center for Blood Diseases, Monash University, 89 Commercial Road, Melbourne 3004, Australia. [∥]These authors contributed equally to this work.

ABSTRACT Neutrophilic granulocytes play a fundamental role in cardiovascular disease. They interact with platelet aggregates *via* the integrin Mac-1 and the platelet receptor glycoprotein Ibα (GPIbα). *In vivo*, GPIbα presentation is highly variable under different physiological and pathophysiological conditions. Here, we quantitatively determined the conditions for neutrophil adhesion in a biomimetic *in vitro* system, which allowed precise adjustment of the spacings between human GPIbα presented on the nanoscale from 60 to 200 nm. Unlike most conventional nanopatterning approaches, this method provided control over the local receptor density (spacing) rather than just the global receptor density. Under physiological flow conditions, neutrophils required a minimum spacing of GPIbα molecules to successfully adhere. In contrast, under low-flow conditions, neutrophils adhered on all tested spacings with subtle but nonlinear differences in cell response, including spreading area, spreading kinetics, adhesion maturation, and mobility. Surprisingly, Mac-1-dependent neutrophil adhesion was very robust to GPIbα density variations up to 1 order of magnitude. This complex response map indicates that neutrophil adhesion under flow and adhesion maturation are differentially regulated by GPIbα density. Our study reveals how Mac-1/GPIbα interactions govern cell adhesion and how neutrophils process the number of available surface receptors on the nanoscale. In the future, such *in vitro* studies can be useful to determine optimum therapeutic ranges for targeting this interaction.

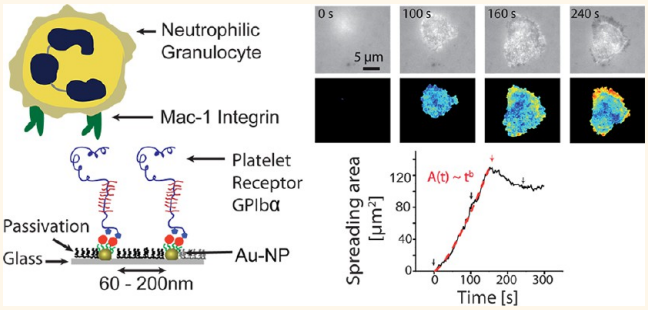

KEYWORDS: biomimetic surfaces · nanopatterning · biofunctionalization · cell adhesion · neutrophils · platelets

The close connection between platelets and cells of the immune system in many fundamental physiological and pathological processes is well-established.[1] Platelets are central protagonists in arteriosclerotic lesions, contributing to leukocyte accumulation and inflammation.[2] Circulating neutrophils and platelet–neutrophil aggregates are increased in patients with coronary artery disease.[3] Leukocyte infiltration at sites of platelet accumulation also occurs after vascular injury.[4] Because elevated neutrophil counts may be associated with cardiovascular risk, the pathophysiological mechanisms are of fundamental medical importance. Novel targeted therapies to disrupt the interaction between neutrophils and platelets could offer an approach to limit cardiovascular damage.

Recruitment of leukocytes to sites of platelet accumulation involves a multistep cascade of adhesive and signaling events.[5,6] These steps include selectin-mediated rolling of leukocytes as well as integrin-mediated firm adhesion and transplatelet migration.[7,8] In particular, the integrin Mac-1 ($\alpha_M\beta_2$ or CD11b/CD18) is responsible for firm leukocyte adhesion to platelets through its interaction with the platelet surface receptor glycoprotein GPIbα (CD42b).[9,10]

As part of the glycoprotein Ib-V-IX complex, GPIbα represents one of the major adhesive receptors on the platelet membrane. The best known function of GPIbα is its interaction with von Willebrand Factor (VWF) at sites of vascular injury and, thus, the initialization of primary hemostasis.[11]

* Address correspondence to spatz@is.mpg.de, michael.schoen@med.uni-goettingen.de.

Received for review July 29, 2013 and accepted October 1, 2013.

Published online October 01, 2013
10.1021/nn403923h

Interestingly, the GPIbα−VWF bond shows high shear resistance, which was attributed as catch bond/flex bond behavior.[12,13] However, GPIbα can also bind to the Mac-1 I domain, which has structural homology with the VWF A1 domain that binds GPIbα.[14]

Even though the GPIb-V-IX complex is constitutively expressed on the platelet surface, its density is dynamic, thus impeding a precise determination of GPIbα distribution *in vivo*. On the one hand, a subset of GPIb-V-IX is thought to be constitutively associated with lipid rafts in unstimulated platelets, and additional copies can be recruited to these microdomains upon stimulation.[15] On the other hand, GPIbα can undergo ectodomain shedding, leading to the release of the soluble extracellular domain, also termed glycocalicin, into the blood, thus reducing the number of available GPIbα binding regions on the platelet surface.[16] Consequently, GPIbα density is a complex biological entity, which can change significantly under different conditions.

Although the importance of the Mac-1/GPIbα interaction has been appreciated, its biological consequences and the required biophysical parameters of this interaction have not been assessed. While *in vivo* models often possess a level of complexity that hinders the isolated and direct observation of a single receptor−ligand interaction, commonly available *in vitro* systems do not allow precise tuning of biophysical parameters such as receptor density and, simultaneously, hydrodynamic shear.

Surface receptors such as GPIbα are laterally distributed within the cell membrane.[17] Nanotechnology can be used to control such chemical features on artificial interfaces. In combination with surface chemistry, tailored surfaces could be designed that mimic biological membranes very precisely. Nanopatterning of biological entities can be achieved by tools such as Dip-Pen nanolithography (DPN), tailored supported bilayers, or block copolymer (micellar) nanolithography (BCML).[18−20] Here, BCML was used to pattern glass surfaces with gold nanoparticles (Au-NPs). In contrast to other methods, this method can precisely control the distance (local density) and not only the global density between the Au-NPs on the nanoscale.[21−23] Such inorganic nanoparticles can be further used as anchor points to bind single proteins in a site-directed manner and defined orientation, which is necessary to mimic the ligand presentation in the cell membrane itself.[24,25]

We have developed a highly tunable *in vitro* model system in which platelet GPIbα was nanoscopically presented at different, locally defined densities. These surfaces mimic the distribution of GPIbα on platelets. The nanostructuring method was used to tune GPIbα densities/spacings in the physiologically relevant range over 1 order of magnitude. Our model surfaces were integrated into a microfluidic setup and allowed the precise study of the Mac-1 integrin-dependent biological responses of human neutrophils with surface-bound GPIbα with or without flow.

RESULTS

Development of Nanostructured Surfaces That Present GPIbα at Precisely Defined Spacings/Densities. The distribution of GPIbα on a platelet surface was mimicked by using a combined nanopatterning/biofunctionalization approach (Figure 1a,b). To gain control over the density and lateral distribution (spacing) of gold nanoparticles (Au-NPs), we used block copolymer micellar nanolithography (BCML) as a nanopatterning method.[21] In short, glass surfaces were dip-coated in a solution of gold-loaded block copolymer micelles, which self-assembled into a quasi-hexagonal pattern. By varying the coating conditions and the block copolymer length, the distance between micelles was controlled. Plasma treatment then removed the organic polymer and released individual Au-NPs (6−10 nm in diameter) at defined interparticle spacings. Finally, GPIbα molecules with C-terminal 6-His tags bound to the Au nanoparticles (6−10 nm in diameter) *via* a NTA-thiol-Ni^{2+} system.

We generated Au-NP patterns of three different spacings: 58 ± 1, 97 ± 1, and 198 ± 2 nm (±SEM; for further details, see Supporting Information S1 and S2). In the article, we used the term "60 nm", "100 nm", and "200 nm" for these patterns. The corresponding densities were 314 ± 11, 99 ± 6, and 27 ± 1/μm^2 (±SEM), respectively. Therefore, the surfaces with small, medium, and large spacings overspan 1 order of magnitude with respect to the Au-NP/GPIbα density.

When neutrophils came into contact with a biofunctionalized surface, they adhered to the surface and showed spreading, movement, and pseudopodia activity (Figure 1c,d).

To avoid nonspecific protein adsorption and unspecific cell interactions with the surfaces, we passivated the glass surface between the Au-NPs. For this purpose, we activated the nanopatterned glass surfaces with O_2 plasma and incubated them with PLL-(20 kDa)-*g*-[3.5]-PEG(2 kDa).[26] In the next step, we covalently bound HS-$(CH_2)_{11}$-EG_3-NTA to the Au-NP. The nitrilotriacetic acid (NTA) headgroup can be used for site-directed immobilization of molecules.[24] Next, the surfaces were incubated with a $NiCl_2$ solution to coordinate Ni^{2+} to the NTA groups. In the last step, the human recombinant His-tagged protein GPIbα was bound to the NTA/Ni^{2+} complex.

To verify that this functionalization regimen worked, we used quartz crystal microbalance with dissipation monitoring (QCM-D) on homogeneous gold. Figure 2b depicts frequency changes (Δf) and dissipation (D) upon the binding of the different compounds in the respective solvents. These changes indicate successful binding of HS-$(CH_2)_{11}$-EG_3-NTA NTA to the Au surface, coordination of Ni^{2+}, and finally binding of GPIbα *via* its terminal His_6 sequence.[27] In the last step, functional

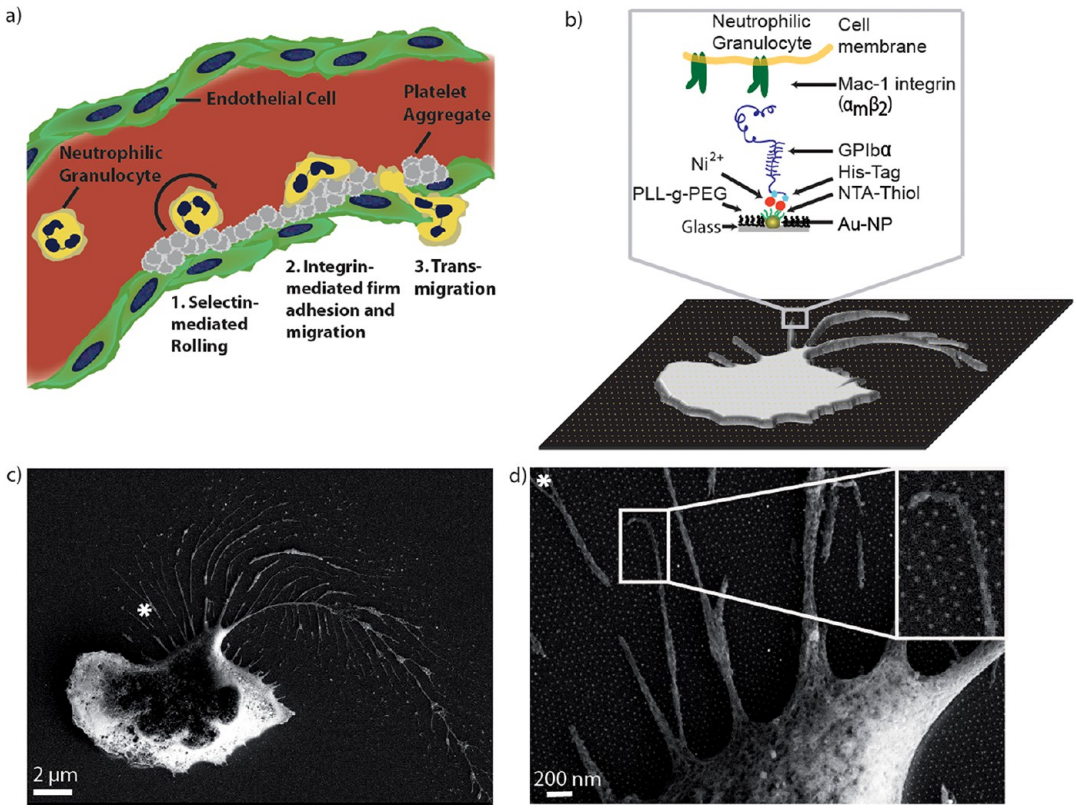

Figure 1. ***In vivo*** **interaction of neutrophils with platelet aggregates and a new** ***in vitro*** **model system. (a) Schematic overview of neutrophilic granulocytes interacting with a platelet aggregate** ***in vivo*****. (b) Experimental setup: GPIbα is immobilized in a site-directed manner** ***via*** **its terminal His_6 group to NTA groups on gold nanoparticles (Au-NPs). Neutrophils expressing the Mac-1 integrin can interact with GPIbα presented on the surface. (c) Scanning electron microscopy (SEM) image of an adhering and migrating neutrophil on such a biomimetic surface. (d) Magnified region with pseudopodia and the functionalized Au-NP pattern in the background. The inset shows a higher-magnification image in which the gold nanoparticles are clearly visible.**

immobilization of GPIbα was verified by binding of an antibody against human GPIbα.

Immunofluorescence microscopy was used to optically verify successful immobilization of GPIbα on the surfaces with Au-NP patterns (Figure 2c). Because of the PLL-*g*-PEG passivation layer between the Au-NPs, neither GPIbα nor GPIbα–antibody adsorbed to areas without Au-NPs.

The low unspecific background of this new *in vitro* model system was confirmed by phase contrast microscopy and RICM. Human neutrophils adhered specifically to nanoscopically presented GPIbα but not to the non-nanostructured area (Figure 2d, e). In the RICM image (Figure 2e), one neutrophil on the border between the nanostructured and the non-nanostructured area of the glass substrate is marked with an asterisk. The part of the cell on the nanostructured side has more black pixels, indicating close contact to the surface, mediated by GPIbα-functionalized nanoparticles.

Model System Allows Highly Specific Neutrophil–GPIbα Interactions. A series of negative and positive controls were used to exclude nonspecific interactions of neutrophils on the biofunctionalized surfaces. Toward this end, human neutrophils were isolated and immediately incubated with the nanostructured surface. Their interaction with the surfaces was recorded for 20 min. The last 40 s of the generated movies were analyzed. Cells were grouped into the categories "inactive" (cells that settled down on the surface without any changes of cell morphology or cells that did not settle down) and "active" (cells that attached/adhered to the substrate and increased their projected spreading area by at least 20% or showed pseudopodia activity on the surface). This binary classification was used to verify the specificity of the biomimetic model system.

On the 60 nm surface, 65.2 ± 6.0% (±SEM, n = 10 donors) of all cells were active (Figure 3b). On the 100 nm surface, 49.1 ± 6.4% (n = 7) belonged to the active group, and on the 200 nm surface, only 22.3 ± 8.1% (n = 7) were active. A significant difference for the proportion of active cells was found when comparing 60 nm *versus* 200 nm (p = 0.002) and 100 nm *versus* 200 nm (p = 0.014). No significant difference could be detected between 60 and 100 nm (p = 0.16; Figure 3a,b).

Nearly all neutrophils were active on the positive control surfaces and inactive on the negative control surfaces (Supporting Information Figure S5 and movies M4 and M5). The glass surfaces that were coated with PLL-*g*-PEG only (without nanoparticles) allowed no interaction of the neutrophils with the surface (inactive).

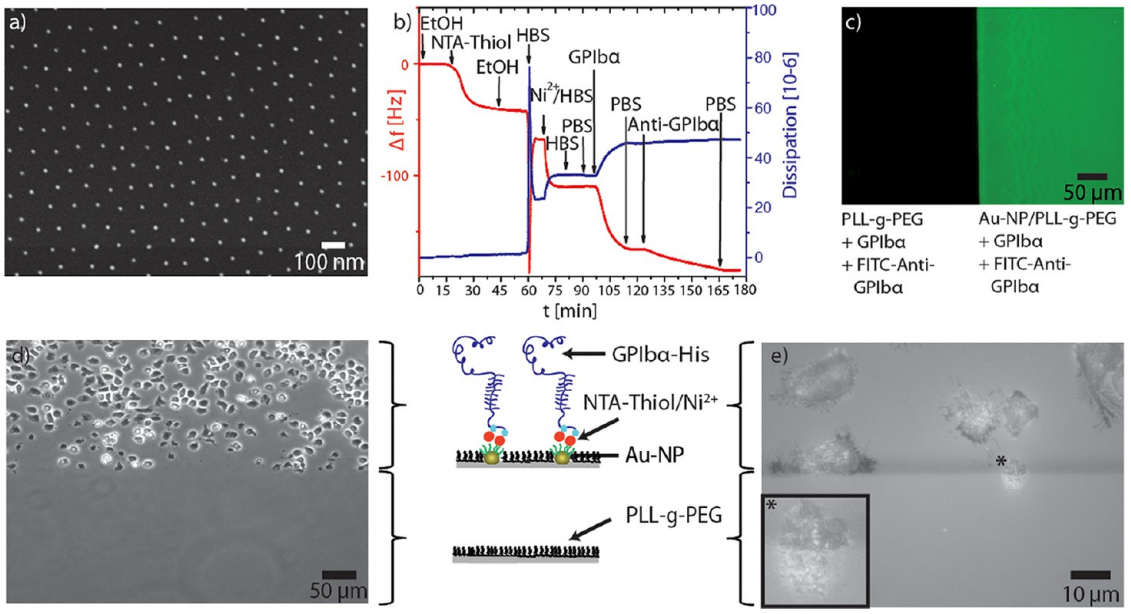

Figure 2. Surface characterization of the biomimetic model system. (a) SEM image of a Au-NP pattern on glass (98 ± 11 nm spacing). (b) Quartz crystal microbalance measurements of the biofunctionalization procedure on homogeneous gold. The frequency/dissipation changes indicate successful conjugation of GPIbα. (c) Immunofluorescence image of the border region between nanostructured and non-nanostructured area. The clear contrast indicates immobilization of GPIbα on the Au-NPs and a low unspecific background. (d) Phase contrast and (e) reflection interference contrast microscopy (RICM) images of neutrophils adhering to the border between the nanostructured and the non-nanostructured area on a sample. The darker pixel values of the neutrophil marked with * indicate closer contact to the area tailored with Au-NPs/GPIbα.

A similar behavior was observed when the neutrophils were incubated with soluble GPIbα prior to the experiment to competitively block Mac-1 receptors on the neutrophils. To show the importance of the binding region for Mac-1 on the surface-bound GPIbα and thereby exclude nonspecific binding of neutrophils to structures on the glass substrates, 60 nm surfaces biofunctionalized with GPIbα were treated for 30 min with a protease isolated from the monocled cobra, *Naja kaouthia* (Nk-protease). Nk-protease specifically cleaves the binding region of GPIbα, leaving a truncated version of the protein on the surface.[28] All neutrophils on these surfaces were inactive (Figure 3c).

As positive controls, neutrophil interactions on glass without nanostructures/passivation and on poly-L-lysine (PLL)-coated glass surfaces were assessed. Both surfaces nonspecifically activated neutrophils, causing an almost immediate and strong morphological change in almost all neutrophils (active). Likewise, when cells were incubated additionally with the activator *N*-formyl-Met-Leu-Phe (fMLP), a potent chemotactic peptide that induces oxidative burst in neutrophils, for 5 min at a concentration of 10^{-6} M prior to the experiment, all cells were active on a 60 nm surface. fMLP-treated neutrophils showed profound morphological changes with a rugged surface and numerous protuberances even before contacting the nanostructured surface.

Dynamics of Cell Adhesion. To learn more about cell surface interactions on the different nanostructured GPIbα surfaces, we used RICM at a wavelength of 470 nm to visualize the interface between the biomimetic surfaces and cell membranes. We analyzed areas of close cell surface contact, spreading kinetics, and cellular mobility. RICM data were collected as 8-bit gray value images with pixel values ranging from 0 (black) to 255 (white), corresponding to distances between cell membrane and surface.[29] The closer the membrane was to the substrate, the darker the corresponding area was in the image. As soon as the cells settled down, they appeared as white objects with darker pixels becoming visible when cells adhered and formed areas of close contact.

The spreading kinetics of neutrophils were analyzed in movies of individual cells (Figure 4a–c). Figure 4a depicts characteristic images of a neutrophilic granulocyte on a 60 nm surface at different time points (top row). The cell first appeared as a white disk, indicating that it was in the proximity of the surface ($t = 0$ s). As the cell settled down, darker patches appeared in the cell surface contact zone, indicating close contact to the nanostructured surface ($t \geq 40$ s). As the cell spread, the spreading area expanded (t = 100 s, 160 s) and more dark regions of close contact emerged. Formation of pseudopodia with a diameter of 200–300 nm started around t = 240 s, with either of the ligand spacings (Supporting Information Figure S6). These pseudopodia could not be discerned in phase contrast or DIC microscopy but were readily observed by RICM and electron microscopy, usually opposite the leading

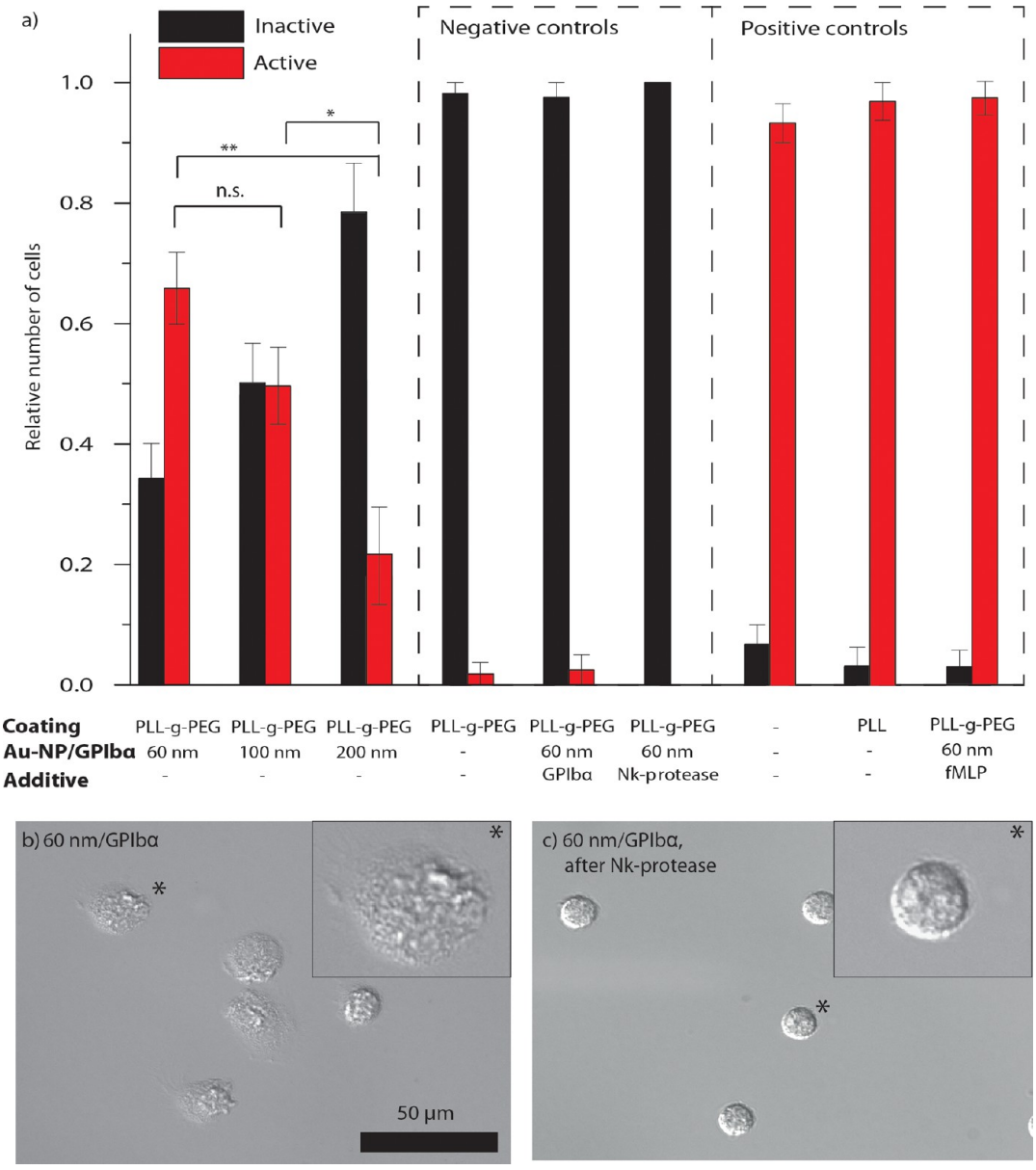

Figure 3. Specific interaction of neutrophilic granulocytes with biomimetic surfaces. (a) Diagram of neutrophil interactions with biofunctionalized surfaces (60, 100, and 200 nm spacing), biological and chemical controls of the experimental system. Errors are SEM, $n \geq 7$ experiments for 60, 100, and 200 nm and $n \geq 2$ for all controls (≥30 cells were analyzed per donor/condition); *$p < 0.05$, **$p < 0.01$ (Mann−Whitney U test). (b) Characteristic DIC images of neutrophils on a 60 nm GPIbα substrate and (c) on a 60 nm surface with a truncated GPIbα molecule (incubation of the surface with Nk-protease before the experiment).

edge of the cell (Figure 1c,d). The middle row of images in Figure 4a shows a binary visualization and the bottom row a translation of RICM pixel gray values into heat maps vividly illustrating close proximity to the surface in red and greater distance in blue.

Spreading area development over time for individual cells was analyzed using a custom-made algorithm that detected cell edges (see Materials and Methods). We defined spreading area as the whole area that is confined by the contour of the cell (see Figure 4a). In Figure 4b, an exemplary growth curve for the neutrophil depicted in 4a is shown. The arrows indicate the time points at which the images from Figure 4a were taken. At the maximum of the growth curve ($t = 160$ s), the phase of initial spreading came to an end. Consecutively, cellular behavior was characterized by the development of pseudopodia, an increase in cellular mobility, and by a slight decrease in cell size (Supporting Information movies M1−M3). To describe the initial spreading phase of the cells, we fitted the spreading areas A to a power law $A(t) \sim t^b$, with time t and growth exponent b, in accordance with analytical descriptions of spreading area kinetics from literature.[30]

This growth exponent depended nonlinearly on the Au-NP/GPIbα spacing (Figure 4c). With a mean value of 2.31 ± 1.50 (standard deviation), the exponent was

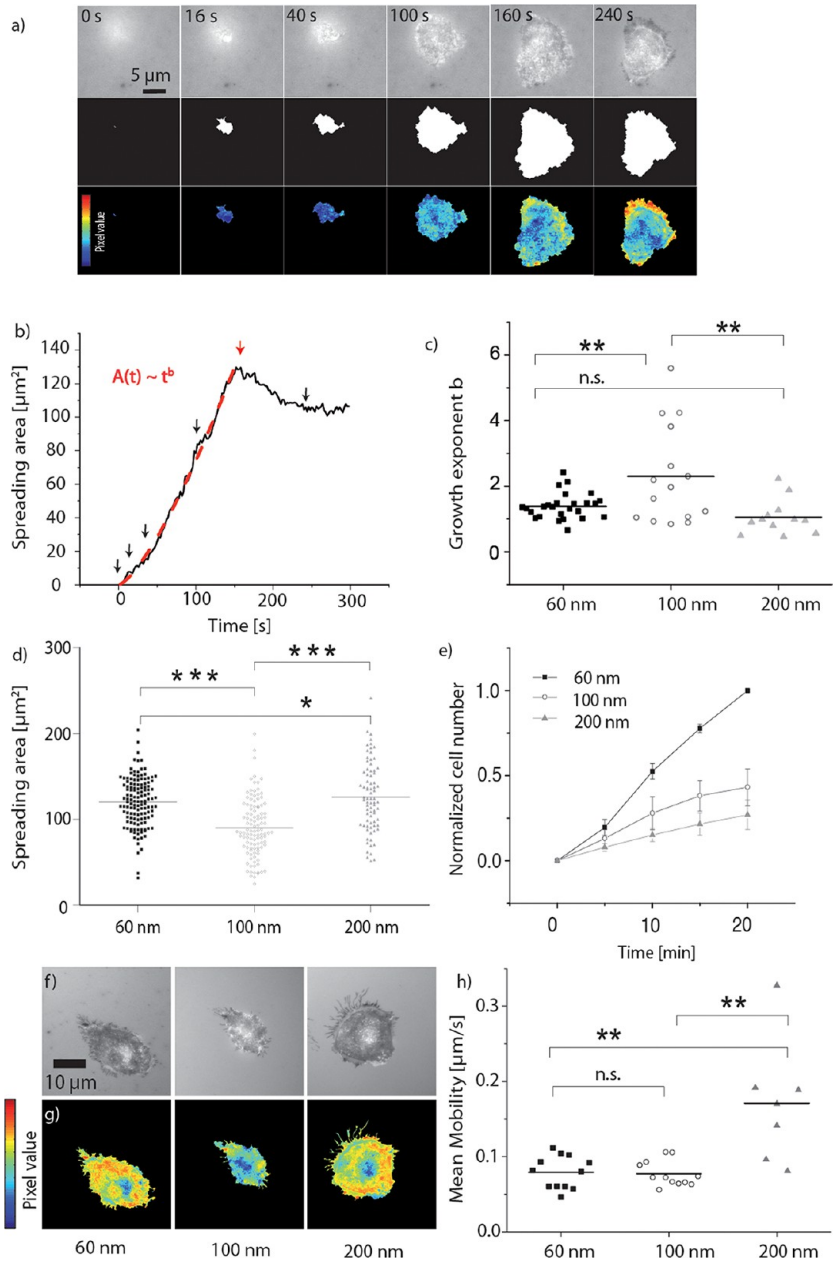

Figure 4. Reflection interference contrast microscopy (RICM) reveals dynamics of neutrophil adhesion on nanoscopic GPIbα. (a) Characteristic time-lapse images of neutrophil spreading on a 60 nm surface over a total of 240 s. The respective images of the cell are RICM images (top line), binary spreading areas of the cell (middle line), and heat maps depicting the relative proximity between cell membrane and surface (bottom line). Red depicts areas of close contact to the surface, and blue indicates greater distance between cell membrane and surface. (b) Spreading area development of the neutrophil shown in (a) on a 60 nm surface (arrows indicate the time points shown in a). The spreading area growth curve during the initial spreading of the cell was fitted to a power law $A(t) \sim t^b$ (red dashed line) up to the onset of movement/pseudopodia activity (red arrow). (c) Diagram of the exponent *b* of the power law fit for the spreading area development of neutrophils on 60 nm ($n = 26$), 100 nm ($n = 15$), and 200 nm ($n = 12$), as indicated; $p = 0.0069$ for 60 *vs* 100 nm, $p = 0.0017$ for 100 *vs* 200 nm, and $p = 0.8258$ for 60 *vs* 200 nm; 95% confidence intervals of the fit were $b \leq 0.05$. (d) Spreading areas of neutrophils after 20 min; $n \geq 337$ cells from 7 donors; $p = 0.0009$ for 60 *vs* 100 nm, $p = 0.0472$ for 60 *vs* 200 nm, and $p < 0.0001$ for 100 *vs* 200 nm. (e) Normalized number of neutrophils adhering with a spreading area of >10 μm^2 (RICM). Errors are SEM ($n = 3$). (f) RICM and corresponding (g) heat map images (depicting cell/surface proximity) of neutrophils on nanoscopic GPIbα (60, 100, and 200 nm spacings) after 20 min. (h) Mean mobility of neutrophils on 60, 100, and 200 nm surfaces; $n \geq 7$ for all cells; $p = 0.0048$ for 60 *vs* 200 nm, $p = 0.0034$ for 100 *vs* 200 nm, and $p = 1$ for 60 *vs* 100 nm. For all statistical analysis, unpaired Bonferroni adjusted *t* tests were used; n.s.: not significant, *$p < 0.05$, **$p < 0.01$, ***$p < 0.001$.

highest on surfaces with 100 nm spacing. On the 60 nm spacings, the growth exponent had a value of 1.39 ± 0.39 and of 1.05 ± 0.53 on the 200 nm spacings ($p = 0.0069$ for 60 *vs* 100 nm, $p = 0.0017$ for 100 *vs* 200 nm). No significant differences were observed between 60 and 200 nm spacings ($p = 0.83$).

To evaluate the cell spreading areas after 20 min (Figures 4d and S4), images from 25 positions of each

sample for each experiment/donor ($n \geq 337$ cells from ≥ 7 donors) were analyzed. The smallest cell adhesion area was found at 100 nm with an average value of 101.6 μm^2 ($p = 0.0003$ for 60 *vs* 100 nm and $p < 0.0001$ for 100 *vs* 200 nm; unpaired *t* test). Between the 60 nm surfaces (mean cellular area 120.21 μm^2) and the 200 nm surfaces (mean cellular area 129.49 μm^2), only a marginal difference could be detected with cells on 200 nm showing a slightly higher average cell area ($p = 0.0157$).

To assess how many cells adhered with close spreading areas, the number of interacting cells was determined as a function of time. Because of the variations of absolute numbers from different donors, the number of cells was normalized to cell count on the 60 nm surfaces after 20 min.

Cells were counted as interacting if they had bright spreading areas >10 μm^2 and at least 10 pixels with gray values smaller than the mean background pixel gray value (dark adhesion patches). At all time points, the cell numbers increased in the order 200 nm < 100 nm < 60 nm (Figure 4e). In Figure 4f, characteristic RICM images of cells on the 60, 100, and 200 nm surfaces are depicted as grayscale images (top row) and as heatmaps (bottom row), indicating areas of different proximity to the surface.

As shown in the movies (M1−M3 and M6), neutrophilic granulocytes produced pseudopodia and entered a phase of random movement on the nanostructured GPIbα substrates following initial spreading. We determined the center of mass of individual cells over the time course of up to 20 min and calculated the mean displacement (as a parameter of mobility). We found the highest mean mobility on the 200 nm surfaces with 0.170 ± 0.081 $\mu m/s$ (standard deviation), while the mobility was significantly reduced both on the 60 nm and the 100 nm surfaces, with 0.079 ± 0.022 and 0.077 ± 0.017 $\mu m/s$, respectively ($p = 0.0016$ for 60 *vs* 200 nm, $p = 0.0011$ for 100 *vs* 200 nm; Figure 4f). No significant difference could be found between the mobility on 60 and 100 nm ($p = 0.8182$ for 60 *vs* 100 nm).

Minimum Receptor Density Is Required To Support Dynamic Cell Attachment under Flow. Experiments under flow conditions were performed to mimic the recruitment of leukocytes to platelet aggregates in the bloodstream. Toward this end, nanostructured surfaces were mounted in parallel plate flow chambers, and the biofunctionalization was performed inside. Neutrophils were injected into the chamber, where they attached/adhered to nanoscopic GPIbα (60 nm spacing, 1 dyn/cm^2) and cell numbers increased linearly with time (Figure 5a). In contrast to static conditions, experiments under flow conditions (1 dyn/cm^2) showed binary differences in the cell response to the spacing. While 100 nm spacings supported cell attachment and activation nearly as well as 60 nm, cell attachment was no longer possible at 200 nm, suggesting a critical threshold spacing between 100 and 200 nm (Figure 5a). Without Au-NPs, the surfaces could not support cell attachment, thus proving the inert background of the PLL-*g*-PEG layer.

The specificity of the interaction under flow was confirmed by two complementary controls: First, the integrin was blocked by incubating neutrophils 30 min before the experiment with mouse anti-human Mac-1 antibody. The number of attached cells decreased by >80%, indicating the crucial role of Mac-1 for the dynamic interaction with GPIbα. Second, cleavage of GPIbα by Nk-protease[28] attested to the GPIbα dependency of the cell binding to the nanostructured surfaces. Indeed, cells could not attach to the truncated form of GPIbα on the nanostructured surfaces (60 nm spacing, Figure 5b), demonstrating that the observed interactions were specifically mediated by GPIbα on the Au-NPs.

The distance-dependent cell attachment could also be shear-stress-dependent, thus creating a system of mutual interference. Therefore, we changed the shear stress conditions incrementally in a physiologically relevant range in flow chambers with different spacings (Figure 5c). At high shear stresses, no (at 10 dyn/cm^2) or very small numbers (at 5 dyn/cm^2) of cells could attach to the surfaces with small (60 nm) and medium spacings (100 nm). At a shear stress of 1 dyn/cm^2, cells attached to small and medium spacings. At a shear stress <0.5 dyn/cm^2 even at 200 nm spacings, cells started to attach to the surface. The slope of the curves in Figure 5c (60 nm, 100 nm) became less steep with decreasing shear stress, which can be explained by the decrease of cell flux (number of cells that pass the surface per time).

DISCUSSION

Despite the fundamental contribution of neutrophil−platelet interactions to many inflammatory pathophysiological situations, no reliable *in vitro* system was available to study precisely how platelet ligands direct neutrophil behavior at the molecular level. We have developed a novel system that allowed the first thorough study of human neutrophils interacting with immobilized human platelet GPIbα, a ligand for integrin Mac-1.[10] This biomimetic model system features site-directed immobilization of GPIbα, leading to an orthotopic orientation of this biomolecule resembling its positioning within the platelet membrane. Furthermore, it provides control over the distance between GPIbα molecules through the precise adjustment of Au-NPs, which serve as anchor points for GPIbα. This GPIbα patterning method therefore allowed control over the local GPIbα density presented at the surface and not just the global density, which is the commonly controlled variable in most conventional *in vitro* assays. The experimental setup models *in vivo* conditions when neutrophils

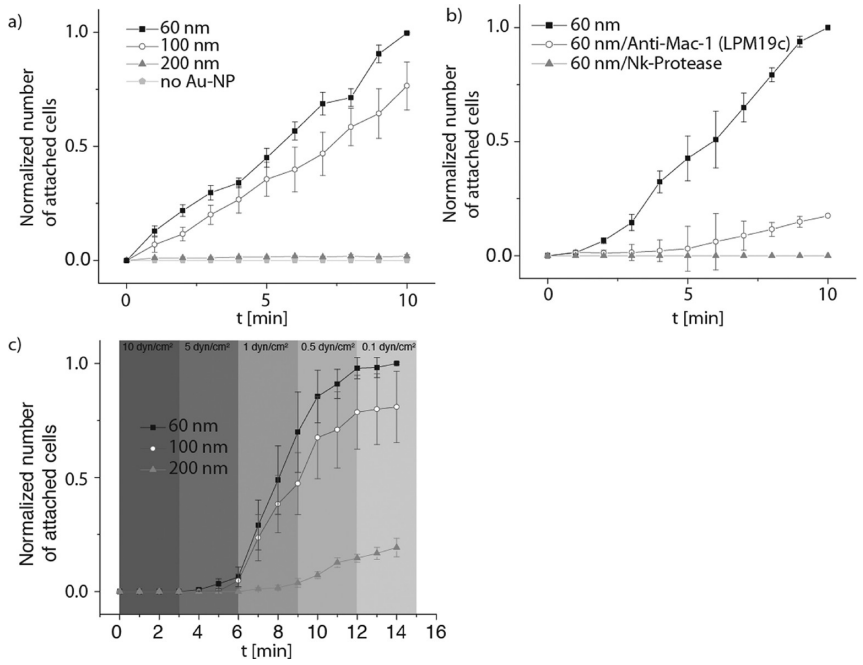

Figure 5. Attachment of neutrophils to nanoscopically presented GPIbα under flow conditions. (a) Neutrophils bound to the nanostructured GPIbα surface under shear stress (1 dyn/cm^2), when the ligand spacing was 60 or 100 nm, whereas without Au-NPs or with a spacing of 200 nm cells did not attach (n = 4). (b) When the Mac-1 integrin was inhibited by a function-blocking antibody, the number of attached cells after 10 min of flow decreased by more than 80%. Cleaving the GPIbα binding pocket by Nk-protease completely abrogated cell binding (shear stress = 1 dyn/cm^2, n = 3). (c) In a shear-stress-dependent and distance-dependent attachment assay, cells attached to the surface when either spacing or shear stress was sufficient to support attachment and resist the shear forces. At shear stress conditions ≥5 dyn/cm^2, no cells or very few attached to the surface for all spacings. For a shear stress ≤0.5 dyn/cm^2, even 200 nm spacings could support Mac-1-dependent attachment to nanoscopic GPIbα (n = 3). Errors are SEM.

start to adhere to platelet aggregates on a thrombus surface.

We studied neutrophil behavior for three different interparticle spacings of GPIbα (60, 100, and 200 nm), resulting in defined ligand densities over a range from 314 to 27 ligands/μm^2. For the first time, we showed a spacing/density dependency of granulocyte functions. The smallest interparticle spacing, 60 nm, is the minimum receptor spacing as estimated from available data (Supporting Information Figure S3). This calculation potentially underestimated the actual distance between the GPIb-V-IX complexes, as we assumed a minimum platelet size and a maximum receptor number for this calculation. Furthermore, the nanoscale distribution of GPIbα can vary considerably as the extracellular domain of GPIbα is shed from the platelet surface upon platelet activation.[16] Thus, it is conceivable that the real *in vivo* receptor spacing lies above this 60 nm minimum value. Moreover, the exact spacing/density might differ between individuals, in different organs or in general in different (patho)physiological situations. The 200 nm spacings corresponded to a receptor density which was more than a factor of 10 lower than on 60 nm spacings (Supporting Information Table S1 and Figure S2). Therefore, these three different Au-NP/GPIbα spacings/densities were likely to span the biologically relevant range of GPIbα densities and can be further refined in the future as receptor densities are more precisely defined.

Given that the proof of biological specificity is a major challenge for all *in vitro* systems, we first focused on proving that this biomimetic surface mediated specific interactions between neutrophils and GPIbα. Indeed, complementary positive controls including immediate spreading of neutrophils on glass, on PLL, or on a 60 nm/GPIbα surface after stimulation with fMLP provided strong circumstantial evidence for the specificity of the molecular interaction in our system. In addition, negative controls showing reduced adhesion after cleavage of the binding region of GPIbα by the specific Nk-protease, after competitive blocking of Mac-1 by soluble GPIbα or when neutrophils came in contact only with the passivating PLL-*g*-PEG, ruled out nonspecific interactions of neutrophils with the biomimetic surfaces. Therefore, this system can serve as a very simplified but specific and chemically well-defined model of a platelet aggregate surface.

We used RICM to visualize adhesion maturation of neutrophils on these biomimetic surfaces. RICM is an ideal method for the analysis of the complex adhesion kinetics of cells and to study cellular behavior in detail.[29−31] Here, it provides information about the distance between cell membrane and substrate (Figure 4a).

The number of adhering cells on the nanostructured surfaces showed a clear dependency of the GPIbα

spacing/density, as expected. The more biomolecules the cells had access to, the more cells interacted successfully with the surface (cell numbers on 60 nm surfaces were 4-fold higher compared to 200 nm surfaces; Figure 4e).

Surprisingly, if neutrophils attached to the surface, their activity did not show the same linear dependency on GPIbα spacing/density, but rather a very robust adhesion behavior. Thus, we could show that neutrophils exhibited very similar spreading kinetics on 60 and 200 nm and the fastest spreading kinetics on 100 nm surfaces (Figure 4c) in spite of a 3-fold lower protein availability than on the 60 nm surface. In addition, the cell spreading area, as determined by RICM, was the smallest on the 100 nm surfaces (Figure 4d).

It is noteworthy that on 200 nm cell spreading area and spreading kinetics were similar to the 60 nm surfaces, although the ligand density on these surfaces was about 10-fold reduced. At least two hypotheses, which are not mutually exclusive, could explain these unexpected observations: First, there might be a nonlinear integration of the number of surface cues and respective signaling. If cells "see" less GPIbα, they would have smaller spreading areas (100 nm, Figure 4d), but if there are too few GPIbα molecules, cells compensate the need for surface cues by changing how signals are integrated/transduced. Another explanation could be a density-dependent selection of neutrophils. While most neutrophils were not able to adhere and spread on a 200 nm surface (smaller cell numbers in Figure 4e), those that adhered functioned normally even on very large interparticle spacings.

In general, the result that only one-tenth of the GPIbα occurring naturally on nonactivated platelets is sufficient to induce neutrophil adhesion and spreading kinetics generally shows that the interaction of Mac-1 with GPIbα is very robust.

In vivo, this could be significant under the different physiological and pathophysiological conditions where platelets become activated and/or shed a portion of their GPIbα receptors off the surface. According to our findings, even aggregated platelets with low GPIbα surface expression would permit neutrophil adhesion, a prerequisite for the initiation of inflammatory processes. Furthermore, the faster spreading kinetics at the 100 nm interparticle spacing implies that a certain degree of receptor shedding could precipitate neutrophil spreading on GPIbα.[32]

Neutrophils that attached to and spread on the 200 nm surface visibly showed more random movement and had a significantly higher mobility as compared to the 60 nm or the 100 nm surfaces (Figure 4h). The increase in cellular mobility is conceivably due to the "need" of the cells to engage ligands on the substrate, to maturate adhesion, and thus to ensure signaling events. From a biophysical point of view, cells would need higher detachment forces for higher densities of ligand−receptor interactions (60 nm) than for a lower number of ligands.

In vivo, the interactions described here would not take place under standardized low-flow conditions but rather under variable shear stress conditions, so the shear dependence of neutrophil adhesion is of central importance. There was a threshold for successful attachment/adhesion under shear stress (Figure 5). At 1 dyn/cm^2, neutrophils readily attached to surfaces with a 60 and 100 nm but not on a 200 nm Au-NP/GPIbα spacing. When the shear stress was increased to over 5 dyn/cm^2, no cells could attach, regardless of ligand density. Conversely, below 0.5 dyn/cm^2, even 200 nm spacings supported neutrophil attachment. These findings suggest the requirement of a minimum number of Mac-1/GPIbα bonds to resist the shear stress.

This dichotomous behavior implies that a certain cellular behavior can be changed by an additional external stimulus such as flow. For all spacings, more cells attached at lower shear stress. In contrast to the well-studied GPIbα/VWF interaction,[12] we did not observe a shear resistance effect under medium shear stress conditions.

When evaluating the results obtained under flow conditions, it is important to consider that neutrophil adhesion to vessel surfaces is mediated by a complex cascade.[7,8,33] Given that integrin interactions are usually preceded by selectin-mediated rolling of neutrophils, the actual shear forces assailing the GPIbα/Mac-1 interaction *in vivo* probably fall below the values estimated from the blood flow velocity. As the actual shear forces applying in any given (patho)physiological microenvironment are challenging to calculate and imitate, the truth about neutrophil behavior on different GPIbα surfaces probably lies somewhere between the *in vivo* measurable shear stress and our low-flow experiments.

We identified several characteristics of cell adhesion that linearly depended on the ligand density, while other hallmarks of cell adhesion showed minimums and maxima at medium ligand densities (Figure 6). From a medical point of view, it is important to know that blockade of a certain number of receptors or ligands does not automatically lead to diminished function of the targeted cells. On the contrary, blocking an insufficient amount of receptors might even lead to a "paradoxical" increase of some cellular functions.[4,34] According to our results, any medication targeting GPIbα platelets would have to ensure a blockade of GPIbα by more than 90% (compared to the density on resting platelets).

These findings are especially interesting in light of the limited success that blockade of integrins has had in treating inflammatory diseases. Conversely, activation of the integrin receptor Mac-1 by small molecule

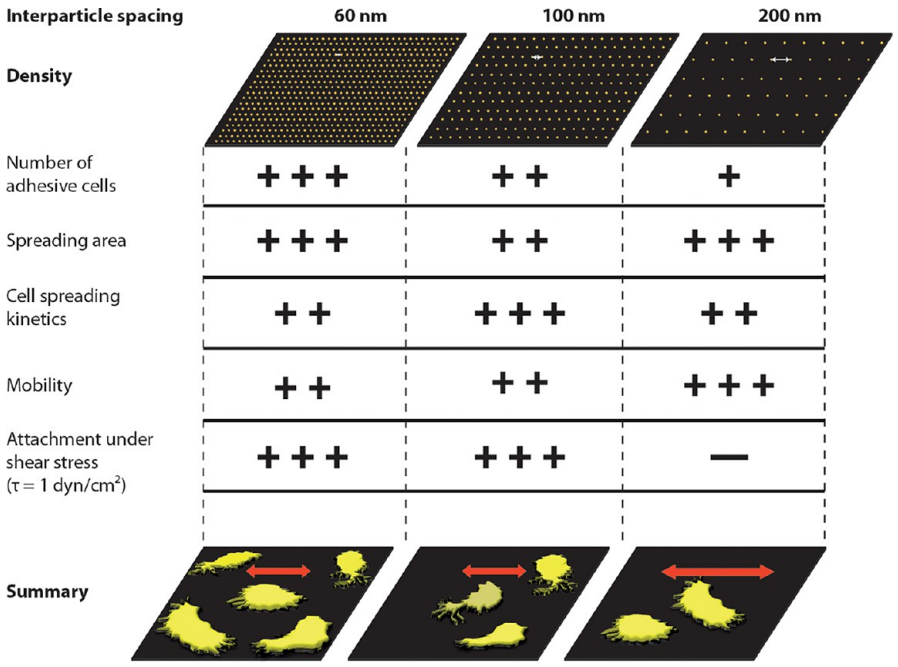

Figure 6. Synopsis of characteristic neutrophil adhesion hallmarks on nanoscopically presented GPIbα. The density/spacing (60, 100, and 200 nm) of the gold nanoparticles carrying GPIbα is visualized schematically in the correct quantitative ratio in the first row. White arrows illustrate the interparticle spacing. The relative degree of cell adhesion and cell morphologies is indicated. A change of 1 order of magnitude in GPIbα density distinctly modulates cellular adhesive behavior which is, however, surprisingly robust. Conversely, under flow conditions (shear stress $\leq$1 dyn/cm^2), a threshold density is necessary to support cell attachment. In summary, a complex interplay of GPIbα ligand density/spacing and shear stress determines distinct functional states of neutrophils. Red arrows represent degrees of cellular mobility.

agonists can, in turn, inhibit neutrophil adhesion and tissue recruitment through ICAM-1 even more efficiently than Mac-1 inhibition.[4,35]

Likewise, antitumoral therapeutics targeting the receptor recognition motif Arg-Gly-Asp (RGD)[36−39] have, at low concentrations, led to an unexpected adverse effect: they stimulated tumor growth and angiogenesis.[34] These notions emphasize that inhibition and activation of surface receptors may follow a complicated concentration-dependent balance.

CONCLUSIONS

We developed a biomimetic model system of the platelet surface and studied human neutrophil adhesion by changing the parameters of ligand density and shear stress. Nanopatterning with Au-NPs and site-directed immobilization provided a precisely defined surface chemistry that allowed us to investigate the specific interaction between neutrophils and surface-bound GPIbα through the integrin Mac-1. This new and versatile platform was used to determine biophysical characteristics and the first response map for neutrophil adhesion on a biomimetic platelet-like surface. We showed that there is a complex relationship between GPIbα density and neutrophil spreading kinetics, spreading area, mobility, and cell attachment under flow. In addition, our results suggest that neutrophil Mac-1-dependent adhesion (without flow) to GPIbα is very robust in terms of GPIbα density. We believe these findings may be of substantial importance for understanding how cells integrate signals from surface cues, the detection of the optimum therapeutic range of novel pharmaceuticals, and the tailoring of individualized therapies.

MATERIALS AND METHODS

Nanopatterning. Nanostructured surfaces were fabricated by using block copolymer (micellar) nanolithography (BCML).[21] The extensive procedure is described in the Supporting Information. We used the terms 60 nm, 100 nm, and 200 nm for surfaces from batches with a spacing of 58 ± 1, 97 ± 1, and 198 ± 2 nm (see Supporting Information S1 and S2). Spacings correspond to densities of 314 ± 11, 99 ± 6, and 27 ± 1/μm^2 ± standard error of the mean (SEM).

Experimental Setup and Biofunctionalization. Cell experiments were performed in flexiPERM (8 chambers, Greiner bio-one, Germany) cell culture chambers or in ibidi parallel plate flow chambers (sticky slides, 0.1 mm height, ibidi, Germany). Nanostructured and plasma-cleaned (10 min/150 W O_2 plasma, TePla 100, PVA, Germany) glass surfaces were mounted on the bottom of the flexiPERM system or the ibidi parallel plate flow chamber. Then the chambers were incubated in 0.5 mg/mL PLL(20 kDa)-*g*-[3.5]-PEG(2 kDa) (SuSoS, Switzerland) in 10 mM HEPES (4-(2-hydroxyethyl)-1-piperazineethanesulfonic acid; Calbiochem, Germany) at pH 7.4 for 45 min. Afterward, the chambers were incubated with 1 mg/mL HS-$(CH_2)_{11}$-EG_3-NTA (NTA = nitrilotriacetic acid; Prochimia, Poland) in ethanol for 90 min. Then Ni^{2+} was bound to the NTA group by incubating the surfaces 20 min with 10 mM of $NiCl_2$ (Merck, Germany) in

HBS (10 mM HEPES, 75 mM NaCl (Roth, Germany), pH 7.5). Finally, the chambers were incubated with 10 μg/mL GPIbα with a C-terminal 6-His tag (rhGPIbα ectodomain, NS0-derived, R&D Systems, Germany) in PBS for 2 h. The chambers were equilibrated in the corresponding solvent before and washed two times with the corresponding solvent for 5 min after each functionalization step.

Surface Characterization. For quartz crystal microbalance with dissipation (QCM-D) measurements, an E4 System (Q-Sense, Sweden) was used. Gold-coated quartz crystals (4.95 MHz, Q-Sense) were cleaned for 45 min/150 W in O_2 plasma (TePla 100). We used the same molecules and solvents for the characterization and biofunctionalization (see section above). To obtain immunofluorescence images, surfaces were incubated for 2 h with 10 μg/mL fluorescein-conjugated mouse anti-human GPIbα IgG antibody (clone HIP1, BD, Germany) in PBS to label GPIbα and verify biomolecule conjugation to the Au-NPs.

Neutrophil Isolation. Neutrophils were isolated from the blood of healthy donors who had not taken medication for at least 10 days. We obtained informed consent from all donors after explaining the nature and the possible consequences of the study. Isolation was performed according to standard protocols.[40] All media used were sterile and endotoxin-free.

In short, 6 mL of venous blood was drawn in a syringe filled with 1 mL of citric buffer (25 g of trisodium citrate dihydrate, 12.8 g of citric acid, 20 g of anhydrous D-(+)-glucose, all from Sigma Aldrich, in 1 L of H_2O, pH 7.4). Blood was mixed with a dextran solution (3% (w/v) Dextran 500 in 0.9% NaCl, both Sigma Aldrich) by gentle inversion and left at room temperature for 20 min for sedimentation of red blood cells. Supernatant from dextran sedimentation was collected and centrifuged at 500*g* for 10 min at room temperature (RT). Supernatant was discarded, and the pellet was resuspended in 35 mL of sterile PBS (Gibco, Invitrogen GmbH, Germany). Ten milliliters of Ficoll-Paque Plus (GE Healthcare, Germany) was carefully layered under the suspension and centrifuged for 40 min at 400*g* at RT. Supernatant except for the pellet containing neutrophils and erythrocytes was discarded. The remaining pellet was resuspended in 10 mL of sterile, distilled water for hypotonic lysis, followed by the addition of 10 mL of sterile 1.8% NaCl solution (Sigma Aldrich, Germany). The solution was centrifuged at 500*g* for 5 min at RT, suspended in 3 mL of HBSS without Ca^{2+}/Mg^{2+} (Lonza), counted, and suspended at 1×10^6 cells/mL. Cells were only used for experiments if >90% had a rounded, quiescent morphology. Experiments were carried out within 2 h of neutrophil isolation. Cellular identity was confirmed by cytospin in combination with a modified Wright-Giemsa staining (Sigma Aldrich). Double staining with both anti-CD16 and anti-Mac-1 in flow cytometry showed a coexpression of both markers in over 99% of the cells, confirming their identity as neutrophilic granulocytes (data not shown).

Cell Experiments. For static experiments in the flexiPerm system, the wells were filled with 400 μL of sterile, endotoxin-free HBSS containing Ca^{2+}/Mg^{2+} (Lonza) at room temperature. To provide a final concentration of 2×10^5 cells/mL, 100 μL of the cell solution with 10^6 cells/mL was added. Immediately after addition of the cell solution, reflection interference contrast microscopy (RICM) or differential interference contrast (DIC) microscopy was performed.

For dynamic flow chamber experiments, cells were also diluted in HBSS containing Ca^{2+}/Mg^{2+} at 2×10^5 cells/mL in a 12 mL syringe mounted in a Al-100 syringe pump (World Precision Instruments, Germany). Cells were then transfused through the flow chamber system at the indicated shear flow. Movies of the field of interest were recorded, and the number of attached cells was determined as a function of time (>60 cells per field of view for 60 and 100 nm surfaces). As the absolute numbers of attached cells varied from donor to donor but the ratio of attached cells between the three substrates was always similar, we normalized the number of attached cells. The highest number of attached cells (the number on 60 nm after 20 min) was set as 1.0, and all other numbers were calculated in relation to this.

Nk-protease to specifically cleave the binding domain of GPIbα off the surface was purified as previously described.[28] The lyophilized protease (0.48 mg/mL in 0.01 M Tris-buffer, 0.15 M NaCl, pH 7.4) was reconstituted in distilled water. For cleavage of GPIbα, the biofunctionalized surfaces were incubated with a 1:50 dilution of protease (0.01 mg/mL, final concentration) in HBSS with Ca^{2+}/Mg^{2+} (Lonza) for 30 min at RT and then washed with HBSS.

For competitive blockade of Mac-1 in static experiments, the stock solution of neutrophilic granulocytes was incubated with a final concentration of 13 μg/mL of soluble GPIbα in HBSS without Ca^{2+}/Mg^{2+} for 5 min prior to the experiment. For activation of neutrophils, cells were incubated with the chemotactic peptide *N*-formyl-Met-Leu-Phe (fMLP; Sigma Aldrich, Germany) at 10^{-6} M for 5 min at RT prior to the addition of the neutrophils to the nanostructured surfaces. For blockade of Mac-1 in the flow chamber experiments, 1 mL of the cell solution (10^6 neutrophils/mL) was incubated with 10 μL of mouse anti-human anti-CD11b antibody solution (Dako, Germany, C3bi, clone 2LPM19c, 100 mg/mL)[10,14] in HBSS without Ca^{2+}/Mg^{2+} (Lonza) for 30 min immediately before the experiment. For experiments under zero-flow conditions, cells were allowed to settle for 2 min. Afterward time-lapse movies were recorded (4 s/frame for DIC, 2 s/frame for RICM) for 20 min. Ten images from random positions were collected at the 20 min time point. In all cell experiments, the order of the used substrates (60, 100, 200 nm, controls) was changed randomly in every experiment to avoid artifacts produced by using slightly older cells.

Microscopy. The RICM setup was implemented on an AxioObserver Z1 inverse microscope with a definite focus option using a 63× Plan NeofluarAntiflex oil immersion objective (NA 1.25; all Zeiss, Germany), a RICM filter cube with a beam splitter (50R/50T VIS) and two polarization filters (AHF, Germany), and a Colibri LED light source (Zeiss) in order to produce coherent monochromatic light to increase the contrast of the interference pattern. The samples were imaged (2 s per frame, 8-bit gray value tiff) at 470 nm with an Orca R2 camera (Hamamatsu, Germany).

DIC microscopy was performed on an Axio Imager microscope with a 40× Plan apochromatic oil immersion objective (NA 1.4) with polarization filters (all Zeiss). Phase contrast and fluorescence microscopy were performed on an Axiovert 200 system and an Axio Imager M1 (Zeiss). Scanning electron microscopy (SEM) was performed using a Zeiss Ultra 55. Sample surfaces with adhering cells were fixed (4% PFA, 10 min) and dried in a critical point dryer.

Data Analysis. We used a customized Matlab (R2009a) routine to detect cells from RICM images and determine cell morphology/spreading area development and center of mass changes. The algorithm was based on standard Matlab image processing functions and was similar to previously described algorithms.[30] First, gray value gradients were detected, and a black−white image was generated, then the image was dilated by linear structuring elements. Finally, the holes were filled, and small objects were removed. Similar data sets were analyzed by using the same threshold parameters. Although the algorithm could not reliably detect pseudopodia, the analysis of initial spreading kinetics was not biased because pseudopodia activity always started after the initial spreading (Figure 4a,b and movies M1−M3 and M6). We defined the spreading area of a cell as the whole area that is confined by the contour of the cell (Figure 4a).

Spreading area growth curves were fitted using the Matlab (R2009a) curve fitting toolbox. RICM movies (2 s/frame) were analyzed starting at one frame before pixels darker than the mean background pixel appeared in the cell/surface contact zone. The end point was the first maximum in the curve, just before migration/movement and pseudopodia activity started. The growth curve was fitted to the function $A(t) \sim t^b$. The fits had 95% confidence intervals $b \leq 0.05$.

For the static analysis of the spreading areas after 20 min, images of the cell body were traced in ImageJ (1.45s, NIH, USA). Pseudopodia were not taken into account.

Cell attachment kinetics under static conditions were evaluated by analyzing RICM movies. The number of interacting cells was counted at different time points on 25 fields of view

(140 μm × 100 μm). A cell was defined as interacting if the bright area (compared to the background) was larger than 10 μm^2 and at least 10 pixels (1 pixel = 0.01 μm^2) of close cell/surface contact were observed in this area. Close contact pixels are defined as pixels with 8-bit gray values smaller than the mean background gray value.

Mobility was assessed by determining the center of mass (Matlab, R2009a) of individual cells from RICM movies after the initial spreading regime. The mean mobility was defined as $= (\Sigma_i|\Delta x_i|)/t$ with Δx_i being the difference between the center of mass of two consecutive frames and a total observation period t (200−300 s). We did not use the term migration because in most cases no directional movement was observed and cells oscillated around the center of mass ($n \geq 7$ for all cells).

Statistical Analysis. For all continuous measurements, a one-way ANOVA was performed to detect differences of the three Au-NP spacings of 60, 100, and 200 nm. If data from multiple cells per donor were available, the donor was considered to be a random factor accounting for potential correlation between measurements from different cells from the same donor. For Figure 3a, donor data were aggregated, and then these summary statistics were analyzed. Further analyses regarding the amount of active and inactive cells were carried out using the Kruskal−Wallis test. If a global effect could be determined, pairwise comparisons were performed using either the independent *t* test or the Mann−Whitney U test. The global type I error rate was 5% with *post hoc* tests adjusted using the Bonferroni procedure to control the level at 5%. All statistical analyses were conducted using SAS 9.3 and Statistica 10 statistical software.

Conflict of Interest: The authors declare no competing financial interest.

Acknowledgment. We thank Vineet Gupta for fruitful discussions, and Lesley Cowan for proofreading. S.K. was supported by PhD fellowships of the Studienstiftung des deutschen Volkes, Fonds der Chemischen Industrie, and HBIGS (Heidelberg University). Part of the research leading to these results received funding from the European Union Seventh Framework Programme (FP7/2007-2013) under Grant Agreement Number NMP4-LA-2009-229289 NanoII and Number NMP3-SL-2009-229294 NanoCARD. This work was funded by the National Institutes of Health (USA) through the Roadmap for Medical Research (PN2 EY016586). J.P.S. is the Weston Visiting Professor at the Weizmann Institute of Science. The financial support of the Max Planck Society is gratefully acknowledged.

Supporting Information Available: Details about the nanoparticle patterns, an estimation of GPIbα densities, time-lapse images (RICM, DIC) of neutrophils on biomimetic and control surfaces, pseudopodia characterization, and RICM movies of neutrophil adhesion maturation. This material is available free of charge *via* the Internet at http://pubs.acs.org.

REFERENCES AND NOTES

1. Zarbock, A.; Polanowska-Grabowska, R. K.; Ley, K. Platelet-Neutrophil-Interactions: Linking Hemostasis and Inflammation. *Blood Rev.* **2007**, *21*, 99–111.
2. Lievens, D.; von Hundelshausen, P. Platelets in Atherosclerosis. *Thromb. Haemost.* **2011**, *106*, 827–838.
3. Nijm, J.; Wikby, A.; Tompa, A.; Olsson, A. G.; Jonasson, L. Circulating Levels of Proinflammatory Cytokines and Neutrophil-Platelet Aggregates in Patients with Coronary Artery Disease. *Am. J. Cardiol.* **2005**, *95*, 452–456.
4. Maiguel, D.; Faridi, M. H.; Wei, C.; Kuwano, Y.; Balla, K. M.; Hernandez, D.; Barth, C. J.; Lugo, G.; Donnelly, M.; Nayer, A.; *et al.* Small Molecule-Mediated Activation of the Integrin CD11b/CD18 Reduces Inflammatory Disease. *Sci. Signal.* **2011**, *ra57*, 1–14.
5. Diacovo, T. G.; Roth, S. J.; Buccola, J. M.; Bainton, D. F.; Springer, T. A. Neutrophil Rolling, Arrest, and Transmigration Across Activated, Surface-Adherent Platelets *via* Sequential Action of P-Selectin and the Beta 2-Integrin CD11b/CD18. *Blood* **1996**, *88*, 146–157.
6. Springer, T. A. Traffic Signals for Lymphocyte Recirculation and Leukocyte Emigration: The Multistep Paradigm. *Cell* **1994**, *76*, 301–314.
7. Alon, R.; Ley, K. Cells on the Run: Shear-Regulated Integrin Activation in Leukocyte Rolling and Arrest on Endothelial Cells. *Curr. Opin. Cell. Biol.* **2008**, *20*, 525–232.
8. Ley, K.; Laudanna, C.; Cybulsky, M. I.; Nourshargh, S. Getting to the Site of Inflammation: The Leukocyte Adhesion Cascade Updated. *Nat. Rev. Immunol.* **2007**, *7*, 678–689.
9. Zago, A. C.; Simon, D. I.; Wang, Y.; Sakuma, M.; Chen, Z.; Croce, K.; Ustinov, V.; Shi, C.; Martinez Filho, E. E. The Importance of the Interaction between Leukocyte Integrin Mac-1 and Platelet Glycoprotein Ib-α for Leukocyte Recruitment by Platelets and for the Inflammatory Response to Vascular Injury. *Arq. Bras. Cardiol.* **2008**, *90*, 54–63.
10. Simon, D. I.; Chen, Z.; Xu, H.; Li, C. Q.; Dong, J.; McIntire, L. V.; Ballantyne, C. M.; Zhang, L.; Furman, M. I.; Berndt, M. C.; *et al.* Platelet Glycoprotein Ibα Is a Counterreceptor for the Leukocyte Integrin Mac-1 (CD11b/CD18). *J. Exp. Med.* **2000**, *192*, 193–204.
11. Berndt, M. C.; Shen, Y.; Dopheide, S. M.; Gardiner, E. E.; Andrews, R. K. The Vascular Biology of the Glycoprotein Ib-IX-V Complex. *Thromb. Haemost.* **2001**, *86*, 178–188.
12. Yago, T.; Lou, J.; Wu, T.; Yang, J.; Miner, J. J.; Coburn, L.; Lopez, J. A.; Cruz, M. A.; Dong, J. F.; McIntire, L. V.; *et al.* Platelet Glycoprotein Ibα Forms Catch Bonds with Human WT vWF but Not with Type 2B von Willebrand Disease vWF. *J. Clin. Invest.* **2008**, *118*, 3195–3207.
13. Kim, J.; Zhang, C. Z.; Zhang, X.; Springer, T. A. A Mechanically Stabilized Receptor-Ligand Flex-Bond Important in the Vasculature. *Nature* **2010**, *466*, 992–1005.
14. Ehlers, R.; Ustinov, V.; Chen, Z.; Zhang, X.; Rao, R.; Luscinskas, F. W.; Lopez, J.; Plow, E.; Simon, D. I. Targeting Platelet-Leukocyte Interactions: Identification of the Integrin Mac-1 Binding Site for the Platelet Counter Receptor Glycoprotein Ibα. *J. Exp. Med.* **2003**, *198*, 1077–1088.
15. Shrimpton, C. N.; Borthakur, G.; Larrucea, S.; Cruz, M. A.; Dong, J. F.; Lopez, J. A. Localization of the Adhesion Receptor Glycoprotein Ib-IX-V Complex to Lipid Rafts Is Required for Platelet Adhesion and Activation. *J. Exp. Med.* **2002**, *196*, 1057–1066.
16. Mo, X.; Nguyen, N. X.; Mu, F. T.; Yang, W.; Luo, S. Z.; Fan, H.; Andrews, R. K.; Berndt, M. C.; Li, R. Transmembrane and Trans-Subunit Regulation of Ectodomain Shedding of Platelet Glycoprotein Ibα. *J. Biol. Chem.* **2010**, *285*, 32096–32104.
17. Andrews, R. K.; Gardiner, E. E.; Shen, Y.; Whisstock, J. C.; Berndt, M. C. Glycoprotein Ib-IX-V. *Int. J. Biochem. Cell Biol.* **2003**, *35*, 1170–1174.
18. Chai, J.; Wong, L. S.; Giam, L.; Mirkin, C. A. Single-Molecule Protein Arrays Enabled by Scanning Probe Block Copolymer Lithography. *Proc. Natl. Acad. Sci. U.S.A.* **2011**, *108*, 19521–19525.
19. Tanaka, M.; Sackmann, E. Polymer-Supported Membranes as Models of the Cell Surface. *Nature* **2005**, *437*, 656–663.
20. Lohmuller, T.; Aydin, D.; Schwieder, M.; Morhard, C.; Louban, I.; Pacholski, C.; Spatz, J. P. Nanopatterning by Block Copolymer Micelle Nanolithography and Bioinspired Applications. *Biointerphases* **2011**, *6*, MR1–12.
21. Spatz, J. P.; Mössmer, S.; Hartmann, C.; Möller, M.; Herzog, T.; Krieger, M.; Boyen, H.-G.; Ziemann, P.; Kabius, B. Ordered Deposition of Inorganic Clusters from Micellar Block Copolymer Films. *Langmuir* **2000**, *16*, 407–415.
22. Lohmueller, T.; Bock, E.; Spatz, J. P. Synthesis of Quasi-Hexagonal Ordered Arrays of Metallic Nanoparticles with Tuneable Particle Size. *Adv. Mater.* **2008**, *20*, 2297–2302.
23. Spatz, J.; Moessmer, S.; Möller, M.; Kocher, M.; Neher, D.; Wegner, G. Controlled Mineralization and Assembly of Hydrolysis-Based Nanoparticles in Organic Solvents Combining Polymer Micelles and Microwave Techniques. *Adv. Mater.* **1998**, *10*, 473–475.
24. Wolfram, T.; Belz, F.; Schoen, T.; Spatz, J. P. Site-Specific Presentation of Single Recombinant Proteins in Defined Nanoarrays. *Biointerphases* **2007**, *2*, 44–48.

25. Sigal, G. B.; Bamdad, C.; Barberis, A.; Strominger, J.; Whitesides, G. M. A Self-Assembled Monolayer for the Binding and Study of Histidine-Tagged Proteins by Surface Plasmon Resonance. *Anal. Chem.* **1996**, *68*, 490–497.
26. Heuberger, M.; Drobek, T.; Spencer, N. D. Interaction Forces and Morphology of a Protein-Resistant Poly(ethylene Glycol) Layer. *Biophys. J.* **2005**, *88*, 495–504.
27. Reviakine, I.; Johannsmann, D.; Richter, R. P. Hearing What You Cannot See and Visualizing What You Hear: Interpreting Quartz Crystal Microbalance Data from Solvated Interfaces. *Anal. Chem.* **2011**, *83*, 8838–8848.
28. Wijeyewickrema, L. C.; Gardiner, E. E.; Shen, Y.; Berndt, M. C.; Andrews, R. K. Fractionation of Snake Venom Metalloproteinases by Metal Ion Affinity: A Purified Cobra Metalloproteinase, Nk, from *Naja kaouthia* Binds Ni^{2+}-Agarose. *Toxicon* **2007**, *50*, 1064–1072.
29. Limozin, L.; Sengupta, K. Quantitative Reflection Interference Contrast Microscopy (RICM) in Soft Matter and Cell Adhesion. *ChemPhysChem* **2009**, *10*, 2752–2768.
30. Sengupta, K.; Aranda-Espinoza, H.; Smith, L.; Janmey, P.; Hammer, D. Spreading of Neutrophils: From Activation to Migration. *Biophys. J.* **2006**, *91*, 4638–4648.
31. Mundinger, T. A.; Sommerfeld, A.; Reinehr, R.; Spatz, J. P.; Haussinger, D.; Boehm, H. Investigating Cell-ECM Contact Changes in Response to Hypoosmotic Stimulation of Hepatocytes *in Vivo* with DW-RICM. *PLoS One* **2012**, *7*, e48100.
32. Wei, S.; Wang, H.; Zhang, G.; Lu, Y.; An, X.; Ren, S.; Wang, Y.; Chen, Y.; White, J. G.; Zhang, C.; *et al.* Platelet IκB Kinase-Beta Deficiency Increases Mouse Arterial Neointima Formation *via* Delayed Glycoprotein Ibα Shedding. *Arterioscler. Thromb. Vasc. Biol.* **2013**, *33*, 241–248.
33. McEver, R. P.; Zhu, C. Rolling Cell Adhesion. *Annu. Rev. Cell Dev. Biol.* **2010**, *26*, 363–396.
34. Reynolds, A. R.; Hart, I. R.; Watson, A. R.; Welti, J. C.; Silva, R. G.; Robinson, S. D.; Da Violante, G.; Gourlaouen, M.; Salih, M.; Jones, M. C.; *et al.* Stimulation of Tumor Growth and Angiogenesis by Low Concentrations of RGD-Mimetic Integrin Inhibitors. *Nat. Med.* **2009**, *15*, 392–400.
35. Faridi, M. H.; Maiguel, D.; Barth, C. J.; Stoub, D.; Day, R.; Schurer, S.; Gupta, V. Identification of Novel Agonists of the Integrin CD11b/CD18. *Bioorg. Med. Chem. Lett.* **2009**, *19*, 6902–6906.
36. Hersel, U.; Dahmen, C.; Kessler, H. RGD Modified Polymers: Biomaterials for Stimulated Cell Adhesion and Beyond. *Biomaterials* **2003**, *24*, 4385–4415.
37. Desgrosellier, J. S.; Cheresh, D. A. Integrins in Cancer: Biological Implications and Therapeutic Opportunities. *Nat. Rev. Cancer* **2010**, *10*, 9–22.
38. Aguzzi, M. S.; D'Arcangelo, D.; Giampietri, C.; Capogrossi, M. C.; Facchiano, A. RAM, an RGDS Analog, Exerts Potent Anti-Melanoma Effects *in Vitro* and *in Vivo*. *PLoS One* **2011**, *6*, e25352.
39. Mitjans, F.; Meyer, T.; Fittschen, C.; Goodman, S.; Jonczyk, A.; Marshall, J. F.; Reyes, G.; Piulats, J. *In Vivo* Therapy of Malignant Melanoma by Means of Antagonists of αv Integrins. *Int. J. Cancer* **2000**, *87*, 716–723.
40. Jutila, M. A.; Walcheck, B.; Bargatze, R.; Palecanda, A. Measurement of Neutrophil Adhesion under Conditions Mimicking Blood Flow. *Methods Mol. Biol.* **2007**, *412*, 239–256.